THE EFFECT OF VEGETATION DENSITY ON CANOPY SUB-LAYER TURBULENCE

D. POGGI, A. PORPORATO and L. RIDOLFI

Dipartimento di Idraulica, Trasporti ed Infrastrutture Civili, Politecnico di Torino, Torino, Italy

J. D. ALBERTSON

Department of Civil and Environmental Engineering, Pratt School of Engineering, Duke University, Durham, U.S.A.

G. G. KATUL

Nicholas School of the Environment and Earth Sciences, Duke University, Durham, U.S.A.

Abstract. The canonical form of atmospheric flows near the land surface, in the absence of a canopy, resembles a rough-wall boundary layer. However, in the presence of an extensive and dense canopy, the flow within and just above the foliage behaves as a perturbed mixing layer. To date, no analogous formulation exists for intermediate canopy densities. Using detailed laser Doppler velocity measurements conducted in an open channel over a wide range of canopy densities, a phenomenological model that describes the structure of turbulence within the canopy sublayer (CSL) is developed. The model decomposes the space within the CSL into three distinct zones: the deep zone in which the flow field is shown to be dominated by vortices connected with von Kármán vortex streets, but periodically interrupted by strong sweep events whose features are influenced by canopy density. The second zone, which is near the canopy top, is a superposition of attached eddies and Kelvin–Helmholtz waves produced by inflectional instability in the mean longitudinal velocity profile. Here, the relative importance of the mixing layer and attached eddies are shown to vary with canopy density through a coefficient α. We show that the relative enhancement of turbulent diffusivity over its surface-layer value near the canopy top depends on the magnitude of α. In the uppermost zone, the flow follows the classical surface-layer similarity theory. Finally, we demonstrate that the combination of this newly proposed length scale and first-order closure models can accurately reproduce measured mean velocity and Reynolds stresses for a wide range of roughness densities. With recent advancement in remote sensing of canopy morphology, this model offers a promising physically based approach to connect the land surface and the atmosphere without resorting to empirical momentum roughness lengths.

Keywords: Canopy turbulence, Closure models, Drag coefficient, Kelvin–Helmholtz waves, Mixing length, Vegetation density, von Kármán streets.

1. Introduction

Vegetation density is known to impact upon many aspects of the flow dynamics within canopies, with direct implications for a suite of physical and biophysical processes (Raupach et al., 1996; Katul et al., 1998; Finnigan, 2000; Horn et al., 2001; Nathan et al., 2002). The density of vegetation canopies is dynamic in space

and time and across a broad range of scales (Scanlon et al., 2002). Hence, the
need to quantify the interdependence between vegetation density and transport
mechanics is now a central problem in meteorology, hydrology, and ecology. This
need has motivated the development and deployment of new remote sensing laser
altimetry, which can map the canopy morphology (Harding et al., 2001; Lefsky
et al., 2002). What is lacking is a robust link between morphological indices and
transport characteristics.

Atmospheric flows near the land surface resemble a rough-wall boundary layer
in the absence of a canopy. However, for a dense and extensive canopy, the flow de-
velops important characteristics of a mixing layer (Raupach et al., 1996; Finnigan,
2000; Marshall et al., 2002). For these two extreme cases (or end members), basic
frameworks exist for quantifying critical attributes of the flow dynamics needed
to describe scalar transport. What is currently lacking is an analogous theory for
intermediate canopy densities in which the flow is neither a purely rough-wall
boundary layer nor a mixing layer (Finnigan, 2000; Novak et al., 2000).

Our objective here is to examine the inter-connection between canopy dens-
ity and key flow statistics within and just above the canopy (hereafter referred
to as the canopy sublayer, or CSL), as needed for quantifying momentum and
scalar transport. Towards this end, flume experiments were used with model can-
opies consisting of regular arrays of vertical cylinders, with variations in cylinder
spacing employed to represent varying canopy densities. We seek a phenomen-
ological theory that describes the key flow statistics in terms of canopy density.
This work is distinguished from previous efforts in that it combines detailed spatial
measurements by non-intrusive laser Doppler anemometry with flow visualization
techniques to arrive at a framework for quantifying the canonical structure of
turbulence in the CSL across a wide range of canopy densities.

2. Experimental Facilities

The experiments were conducted at the hydraulics Laboratory, DITIC Politecnico
di Torino, in a re-circulating flume shown schematically in Figure 1. The main
component of the flume is a rectangular channel 18 m long, 0.90 m wide and 1 m
deep. The walls are made of glass to allow the passage of laser light (Figure 2).

The model canopy is composed of an array of vertical stainless steel cylinders,
0.12 m high ($= h$), and 4 mm in diameter ($= d_r$) equally spaced along the 9 m
long and 0.9 m wide test section. The test section begins 7 m downstream from
the channel entrance. The rods were firmly installed into two parallel steel sheets
drilled with evenly spaced holes. A polyurethane board was placed between the
two sheets to further increase the rigidity of the rods. Here, we focus on five canopy
roughness densities: 67, 134, 268, 536, and 1072 rods m^{-2} which are equivalent to
element area index, EAI (front area per unit volume), values of 0.27, 0.53, 1.07,
2.13, and 4.27 m^2 m^{-3}, respectively. Alternatively, a frontal area index (frontal
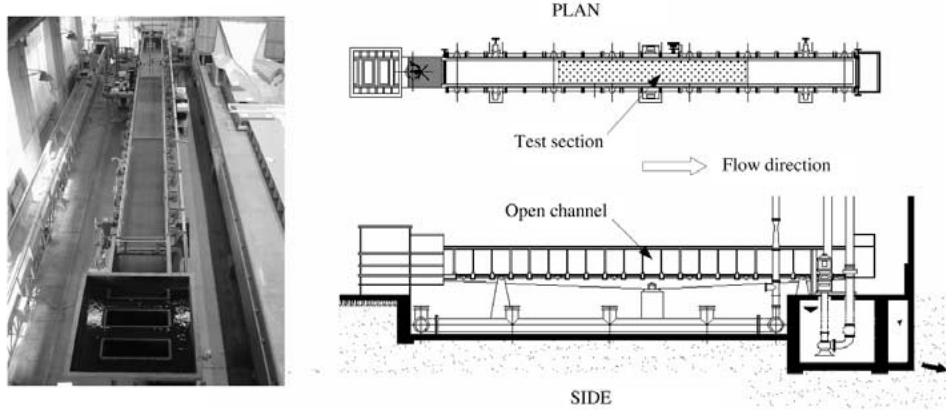
Figure 1. Plan and lateral view of the channel flow facility.

TABLE I

Details of the experimental conditions for various roughness configurations ($D1$ to $D5$). The roughness measures are the element area index (EAI), and frontal area index (a). The velocity scales are the mean longitudinal velocity at $z/h = 1$ (u_h), the friction velocity (u_*), and the bulk velocity or depth-averaged velocity across the entire water depth (u_b). The length scales are canopy height (h), rod diameter (d_r), and water depth (h_w). The relevant Reynolds numbers (Re) are: The Roughness Re, hu_*/ν, Flow Re, $h_w u_b/\nu$, and Element Re, $d_r u_*/\nu$.

	$D1$	$D2$	$D3$	$D4$	$D5$
Rods density (Rods m^{-2})	67	134	268	536	1072
EAI (m^2 m^{-3})	0.27	0.53	1.07	2.13	4.27
a (m^2 m^{-2})	0.032	0.064	0.129	0.256	0.512
u_h (m s^{-1})	0.249	0.232	0.207	0.186	0.147
u_* (m s^{-1})	0.014	0.018	0.023	0.029	0.039
u_h/u_*	0.058	0.076	0.113	0.156	0.269
u_b (m s^{-1})	0.309	0.312	0.313	0.313	0.300
Roughness Re	1615	2076	2653	3346	4500
Flow Re	176000	178000	179000	178000	171000
Element Re	957	892	796	715	565

area per unit ground area), referred to as a, was also used to characterize roughness density (see Table I). Hence, the roughness density varies by a factor of over 20. While we acknowledge that there is no one-to-one correspondence between a and a leaf area density, we note that the a associated with the densest canopy case does induce a drag that is comparable to a dense forest canopy (Katul and Albertson, 1998). By comparison, we mean that the magnitude of a is sufficiently large so
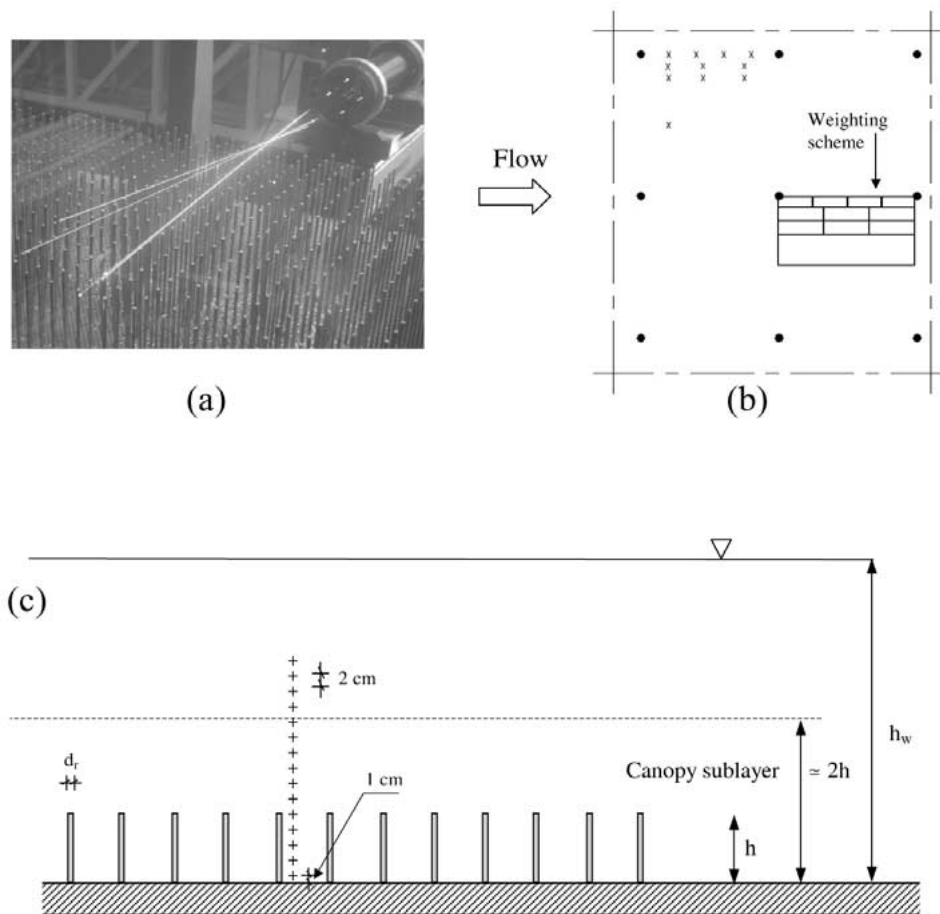
Figure 2. (a) The laser Doppler anemometer (LDA) and rod arrangement in the flume. (b) Plan view of the velocity sampling, circles are the rod positions, crosses are the sampling points of LDA. (c) Same as (b) but for the section view.

that the longitudinal velocity at the top of the canopy, normalized by the friction velocity, attains a value comparable to values reported in canopy sublayer field experiments conducted in dense canopies (discussed in Appendix A).

The velocity was measured by using two-component laser Doppler anemometry (LDA) used in forward scattering mode. A key advantage of LDA is its non-intrusive nature, its small averaging volume, and its ability to measure velocity excursions close to obstacles. The signal processing was performed by two Dantec Burst Spectrum Analyzer (BSA) processors. The coincidence mode was used to obtain more reliable measurements of the Reynolds shear stress. To preserve the correlation coefficient between the vertical (w) and the longitudinal (u) velocity components, all data points not exactly temporally coincident were discarded. Further details about the LDA configuration and signal processing can be found in

Poggi et al. (2002). To compare the flow statistics across different canopy densities, the flow Reynolds number was preserved by varying the volumetric flow rate but retaining the water depth ($= h_w$) at a steady 0.6 m (see Table I).

With the LDA, a measurement run consists of sampling the time series of u and w at a particular position. Given the planar non-homogeneity in the flow statistics within the canopy, 11 measurement locations were used. These 11 locations were not uniformly spaced; rather, they were chosen such that sampling locations were more densely placed in regions where the flow statistics exhibit the highest spatial variability. In Figure 2, the plan view of the locations of the sampling positions are shown relative to the cylinders. At each of the 11 horizontal positions, a profile of 15 vertical measurement locations was established (see Figure 2). The sampling duration for each of the runs was 300 s and the sampling frequency was 2500–3000 Hz. The analog signals from the processor were checked by an oscilloscope to verify the Doppler signal quality at each of the 11×15 runs. No artificial seeding of the channel was employed.

Visualization experiments were also conducted by injecting a fluorescent dye solution (Red Rhodamine) at several vertical layers. The Rhodamine has a faint red colour that becomes metallic green when excited by the laser. A cylindrical lens was used to split the laser beam into a thin sheet and provide a planar illumination at the working section. The laser sheet excited the dye in a pre-set plane and allowed identifying and photographing the dominant vortices at the particular level within the canopy.

3. Results

In this section we first describe the qualitative effects of the canopy density on the basic flow statistics within the CSL, including velocity moments, characterization of ejections and sweeps, and preferential energetic scales. Using this characterization, we proceed to build a phenomenological mixing length model for the CSL applicable to a wide range of roughness densities. Finally, implications to first-order closure models are discussed.

3.1. VELOCITY MOMENTS

When computing the statistical moments, we first time averaged and then planar-averaged to yield vertical profiles, as defined by Raupach and Shaw (1982). The planar averaging at each vertical position was performed using a weighted scheme, with weights proportional to the fraction of total ground area represented by each position (the representative regions are shown in Figure 2). For notational simplicity, and unless otherwise stated, we denote by $\overline{c}$ the time and horizontally averaged value of a flow variable c, and by c' the instantaneous local departures from $\overline{c}$.

Figure 3 shows the measured profiles of the basic turbulence statistics for all five roughness densities. These moments demonstrate how canopy turbulence is trans-
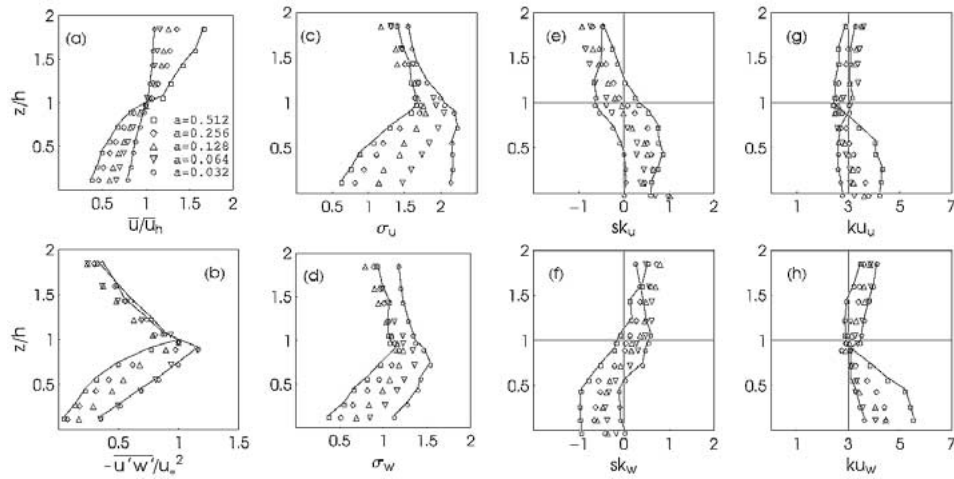
Figure 3. Variation of temporally- and horizontally-averaged moments with normalized height (z/h) for (a) mean longitudinal velocity, (b) mean shear stress, (c) longitudinal velocity standard deviation ($\sigma_u = \overline{u'^2}^{1/2}/u_*$), (d) vertical velocity standard deviation ($\sigma_w = \overline{w'^2}^{1/2}/u_*$), (e-f) longitudinal and vertical velocity skewness ($sk_u = \overline{u'^3}/\sigma_u^3$ and $sk_w = \overline{w'^3}/\sigma_w^3$), and (g-h) longitudinal and vertical velocity kurtosis ($ku_u = \overline{u'^4}/\sigma_u^4$ and $ku_w = \overline{w'^4}/\sigma_w^4$). Solid lines represent the sparsest and densest canopies.

formed from a boundary layer (one end-member) to a flow resembling a perturbed mixing layer (the other end-member) with increasing roughness density. The signature of this shift is apparent through the magnitude of the inflectional instability in the mean velocity profile and through signatures of sweeps and ejections in higher order moments (discussed below).

Mean Velocity. Figure 3a shows the velocity profiles for all the density cases normalized by the velocity at the canopy top (u_h). The most fundamental difference between dense and sparse canopies is the magnitude of the inflection in the mean velocity profile; this inflection is a necessary condition for the occurrence of Kelvin–Helmholtz instabilities and the magnitude of the inflection defines the relative importance of this mechanism to the overall turbulence structure.

Variances. With increasing a, the magnitudes of the root-mean squared longitudinal (σ_u) and vertical (σ_w) velocity are strongly damped for $z/h < 1$. Another supporting observation of the end-member relevance, is that σ_w at the top of the canopy, when normalized by the friction velocity $\left(u_* = -\overline{u'w'}\vert_{z=h}^{1/2}\right)$, shifts from about 1.3 for sparse canopies, which is typical of rough-wall boundary layers, to about 1.1 for dense canopies, which is typical for mixing layers, in agreement with Raupach et al. (1996).

Skewness and Flatness Factors. There is a general trend for the skewness in u to go from positive within the canopy to negative above the canopy. The dense canopies have the stronger positive skewness inside the canopy, suggesting a dom-

inant role played by sweeps of high velocity fluid down into the dense canopy space. Correspondingly, the skewness of w tends to go from negative inside the canopy to positive above the canopy, with the stronger negative skewness for the dense canopy, again suggesting the greater role of sweeps in this setting than in the sparse canopy setting. The sparse canopies have an absence of skewness for both the u and w in the region of $z < h/2$ and maximum skewness magnitude occurs at $z = h$. Contrastingly, the peak skewness magnitudes are deeper into the dense canopies. The skewness measurements indirectly suggest that for sparse canopies sweeps play no prominent role in the exchange of momentum, whereas in dense canopies they do. Analysis of the fourth-order moments for u and w further supports the picture emerging from the skewness results. Both kurtosis of u and w are near Gaussian in the region above the canopy for all densities (where ejection events dominate). Profound dissimilarities exist within the canopy space when contrasting sparse and dense canopies, as shown in Figures 3g, h. These differences in kurtosis (within the canopy) vary clearly with roughness density. When the third- and fourth-order moment results are taken together, the sparse canopy resembles a boundary layer (i.e., near-Gaussian statistics) while the dense canopy experiments document significant departure from Gaussian distributions, a finding consistent with numerous field CSL experiments (Katul and Albertson, 1998). This shift from near-Gaussian to non-Gaussian lends support to the concept of using increasing canopy density as an indicator of flow scaling between boundary layers (sparse canopies) and perturbed mixing layers (dense canopies).

3.2. QUADRANT ANALYSIS

The previous analysis suggests that the region inside the canopy appears to be dominated by sweeping motion for dense canopies while ejections dominate for sparse canopies. To verify this statement, quadrant analysis is used because it provides a more direct quantification of the key attributes of the ejection-sweep cycle.

In quadrant analysis (Lu and Willmarth, 1973), the Cartesian plane defined by w' (ordinate) and u' (abscissa) is divided into four quadrants, with each quadrant contributing to the overall Reynolds stress $\overline{u'w'}$. To isolate the contribution of extreme events within each quadrant, a hyperbolic hole or threshold H is commonly employed (i.e., analysis of all $|u'w'| > H |\overline{u'w'}|$). As such, ejection events are associated with large instantaneous values of $u'w'$ in the second quadrant (i.e., $u' < 0$, $w' > 0$), while sweep events are associated with large instantaneous $u'w'$ values in the fourth quadrant (i.e., $u' > 0$, $w' < 0$). Values of H commonly used in such threshold analysis vary from 3 to 4 (Antonia, 1981; Raupach, 1981; Nakagawa and Nezu, 1977). A common measure to quantify the relative importance of ejections and sweeps to $\overline{u'w'}$ is ΔS_o, given by

$$\Delta S_{o,H} = \frac{\overline{u'w'}_{H,IV} - \overline{u'w'}_{H,II}}{\overline{u'w'}}, \tag{1}$$

where $\overline{u'w'}_{H,IV}$ and $\overline{u'w'}_{H,IV}$ are the Reynolds stresses, in the fourth and second quadrants, respectively, subject to a hyperbolic threshold H. In Figure 4, we show the outcome of the quadrant analysis for dense and sparse canopy densities, for both $H = 0$ (i.e., all the data) and $H = 3$ (i.e., extreme events). It is evident from Figure 4 that the region above the canopy is primarily dominated by ejections irrespective of the canopy density. The momentum flux within the canopy, however, is controlled by weak ejections in sparse canopies (as is the case in boundary-layer flows) and by strong sweeps within dense canopies. This is true when all events ($H = 0$) are considered and when the analysis is focused on extreme events ($H = 3$); these results are also in good agreement with a wide range of field experiments (Katul and Albertson, 1998). In Figure 4c, d, we also show the stress fractions due to sweeps and ejections for all five canopy density cases. Here we see the emergence of a gradual shift from standard boundary-layer flows to canopy flows with increasing canopy density.

Up to this point, the analysis has focused on single-point statistics and how they are influenced by canopy density. We proceed next to assess how the canopy density alters the characteristic length and time scales of the energetic motion.

3.3. Spectral analysis and flow visualization

To explore the dominant energetic time (and length) scales, we utilize flow visualization techniques along with spectral analysis. Flow visualization experiments are conducted within the canopy layers using a horizontal laser sheet (see, for instance, Figure 5a at $z/h = 0.2$). These visualizations suggest that organized motion in these layers is dominated by the classical von Kármán vortex streets. Figure 5a shows a sequence of pictures highlighting the geometric attributes of the 'within canopy' vortices. From the flow visualization, the spatial coherency, periodicity, and the alternating character of these vortices are clear. These predominantly horizontal structures influence vertical transport as evidenced by the spectral analysis of the vertical velocity component, which we discuss next.

The spectra of w for the sparsest and densest canopy conditions are shown in Figure 5b–c. The energy spectra and the frequency are normalized with local mean velocity and rod diameters. The spectra reported here were averaged in the same manner as the velocity moments. The w spectra for four contrasting measurement heights inside the canopy ($z/h = 0.15, 0.29, 0.46, 0.75$) collapse for both the densest and sparsest canopy cases, with a unique secondary peak at dimensionless frequency $f d_r/\overline{u} = 0.21$, where d_r is the rod diameter. This is not surprising given that 0.21 is the classical Strouhal number ($= f d_r/\overline{u}$) linking frequency of periodic vortices to the mean velocity and the characteristic length scale of the obstacle (for vertical columns). The Strouhal number is approximately constant across a wide range of Reynolds numbers ($d\overline{u}/\nu = 60$ to 5000, Schlichting, 1979). More importantly, for $z/h < 1$ this secondary spectral peak appears independent of a and z/h.
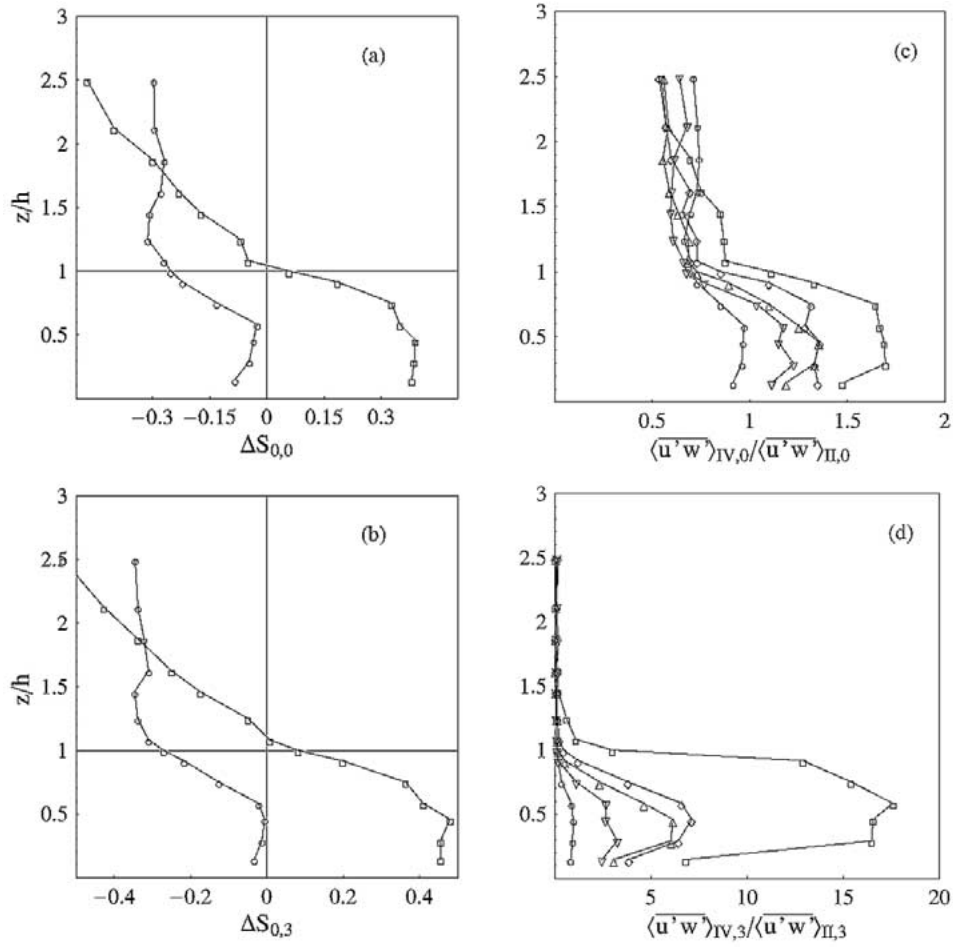
Figure 4. $\Delta S_{0,H}$ for the densest ($\square$) and sparsest ($\bigcirc$) canopy density: (a) $H = 0$; (b) $H = 3$. In (c), (d) are shown the stress fractions due to sweeps and ejections and for all the canopy density measurements. See Figure 3a for canopy density code.

Such secondary peaks are also connected with the classical spectral short-circuit process (Kaimal and Finnigan, 1994; Finnigan, 2000) in which large turbulent eddies are broken and have their energy short-circuited to scales comparable to the wakes behind individual canopy elements. The short-circuiting is difficult to detect in traditional CSL field experiments for two reasons: (1) The multiplicity of the geometric scales (e.g., stems, branches, leaves) of real canopies, which are absent in our experiments, and (2) the wide use of sonic anemometers, which have path lengths larger than the scale of the canopy elements producing the wakes. The use of LDA removes such volume-averaging limitations imposed by sonic anemometers.
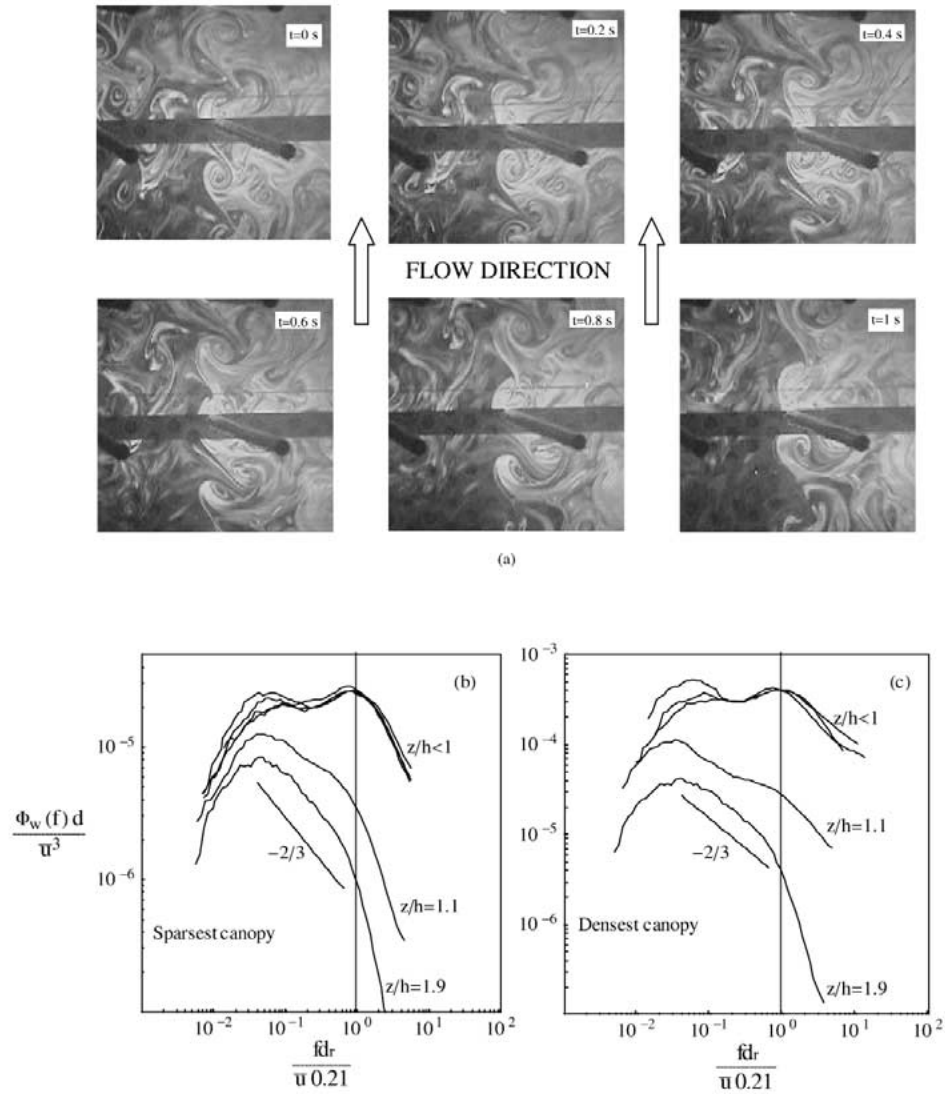
Figure 5. A short sequence of vortices behind a rod (a). The vertical velocity spectra Φ_w, normalized by rod diameter, d_r, and $\overline{u}$ as a function of dimensionless frequency, are shown for the sparsest (b) and densest (c) canopies.

From both the visualization and the spectral analysis it is clear that the region inside the canopy, irrespective of a and z/h, is dominated by energetic motions controlled by length scales reflecting the local canopy geometry (i.e., proptional to d_r in this case). It is important to note that the flow visualizations are conducted for the densest canopy thereby resulting in smaller local element Reynolds numbers when compared to sparser canopies. Whether these element Reynolds numbers

are sufficiently high may be questioned given the degree of organization in the vortical structure observed from the flow visualization. Despite these observations, the spectral analysis suggests that the Reynolds number may be sufficiently high even for the dense canopy. Notice that the spectra for the sparse and dense canopies at the deeper layers are qualitatively the same despite the large differences in the local element Reynolds number ($Re_d = \overline{u}d_r/v$).

4. Phenomenological Model

Thus far, our analysis of the measured statistical moments and ΔS_o suggests that sparse canopies resemble boundary layers while dense canopies share many attributes with perturbed mixing layers, at least near $z/h = 1$. Furthermore, a is shown to be an appropriate scaling parameter describing the shift between rough-wall boundary layers and perturbed mixing layers in this region. Hence, our conceptual model for the CSL is that for intermediate canopy densities, the turbulent mixing length in the vicinity of $z/h = 1$ is a superposition of values representing boundary layers and mixing layers, with the superposition weights defined by canopy density. Furthermore, well above the canopy ($z/h \gg 1$), the mixing length model must converge to the canonical rough-wall boundary layer value, irrespective of a.

Deeper in the canopy ($z/h < 1$), spectral analysis suggests that the energetic motion is dominated by von Kármán vortex streets and hence the mixing length is strictly dependent on d_r and independent of a.

In essence, three flow types dominate the mixing-length properties within the CSL: von Kármán street, rough wall boundary layer, and mixing layer. We review the canonical length scales associated with these flows, prior to building a composite mixing-length model for the entire CSL.

We begin by recalling that the region deep within the canopy ($z/h \ll 1$) is characterized by von Kármán vortex streets with a vortex size (L_V) proportional to d_r, as established above, and independent of a and local velocity. In boundary layers, the characteristic length scale of vortices (L_{BL}) scales with the distance from the wall. The main hydrodynamic attribute of mixing layers is the strong inflection in the velocity profile, which, through the Kelvin–Helmholtz instability, induces transverse vortices of size L_{ML}. In summary, the typical vortex size for each of the three flows can be expressed as

$$
\text{Vortex size} \begin{cases} L_{BL} = (z - d) & \text{boundary layer (inner region)} \\ L_{ML} = 2L_s = 2(\overline{u}/(\mathrm{d}\overline{u}/\mathrm{d}z))_{z=h} & \text{mixing layer} \\ L_V = \overline{u}/f = d_r/0.21 & \text{von Kármán street} \end{cases} \text{,}
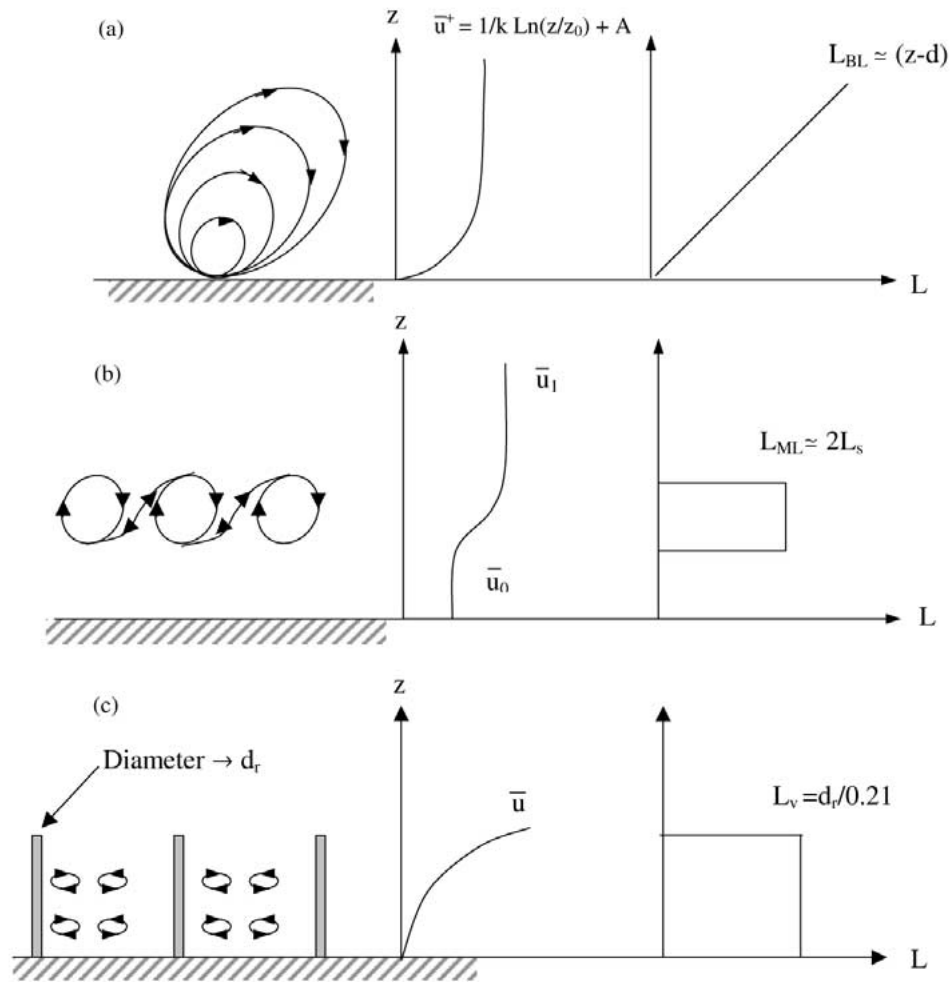$$

Figure 6. Conceptual model for the mixing lengths in different regions within the canopy sublayer. (a) Boundary-layer flow (with k being the von Kármán constant), (b) mixing layer, (c) von Kármán streets.

where d is the zero plane displacement (not to be confused with d_r, the rod diameter), and L_s is the shear length scale. The corresponding mixing lengths associated with these vortex sizes are

$$\text{Mixing length} \begin{cases} l_{BL} = kL_{BL} & \text{boundary layer (inner region)} \\ l_{ML} = L_{ML}/2 = L_s & \text{mixing layer} \\ l_V = L_V & \text{von Kármán street} \end{cases},$$

where k is the von Kármán constant. Figure 6 presents an elementary description of the vortex sizes in the three regions.
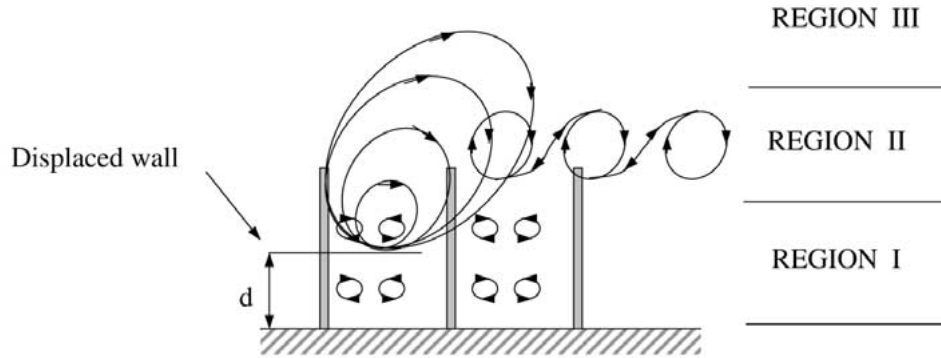
Figure 7. The superposition of three length scales within the canopy sublayer. Region I is primarily driven by von Kármán vortex streets, Region II is a superposition of all three components, and Region III is a displaced rough wall boundary layer.

Thus, our phenomenological model for the CSL assumes that the flow field includes three basic length scales (l_V, l_{ML}, and l_{BL}) with relative weights that vary with z/h and a. A simplified version of the conceptual model is shown in Figure 7. For Region I ($z/h \ll 1$), the flow field is primarily dominated by small vortices associated with the von Kármán streets. Region II, straddles the top portion of the canopy, and is dominated by a mixing layer in the denser canopy cases. Finally, Region III ($z/h \gg 2$) is the classical boundary-layer region dominated by vortices with length scales proportional to ($z - d$).

We emphasize that in region II (see Figure 7), while both Kelvin–Helmholtz and boundary-layer vortical structures contribute to momentum transfer at a given point in space over some averaging time interval, these vortical structure are not likely to co-exist in space. The lack of spatial co-existence is due to the fact that the production mechanism responsible for generating one of them is likely to impede the formation of the other.

These three regions and their inherent vortex length scales form the basis for a closure of the mean momentum equation (described next).

5. Model Formulation

For planar homogeneous and steady-state conditions the mean longitudinal momentum balance reduces to

$$\frac{d\overline{u'w'}}{dz} + \frac{d\overline{p}}{dx} - F = 0, \tag{2}$$

where p is the kinematic pressure, and F is the force vector on a unit mass within the averaging volume. For our experimental setup, $d\overline{p}/dx$ is constant for all runs. This constant was determined from runs conducted with $F = 0$ so that

$d\overline{p}/dx = -d\overline{u'w'}/dz$. The computed pressure gradient was further verified using the measured horizontal gradient of the water surface profile, which for a flat channel, approximates the pressure gradient.

5.1. CLOSURE SCHEMES

In order to derive the mean velocity profile, the following standard closure schemes were adopted:

(1) The aerodynamic force per unit volume is parameterized as

$$F(z) = -\frac{1}{2}C_D(z, Re, a)a\overline{u}|\overline{u}|, \tag{3}$$

where C_D is the drag coefficient.

(2) The classical K-theory model is adopted for the Reynolds stress

$$\overline{u'w'} = -K_M \frac{d\overline{u}}{dz}, \tag{4}$$

where K_M is the eddy diffusivity for momentum.

With these parameterizations, the mean momentum equation becomes

$$-K_M \frac{d^2\overline{u}}{dz^2} - \frac{dK_M}{dz}\frac{d\overline{u}}{dz} + \frac{1}{2}C_D a\overline{u}|\overline{u}| + \frac{d\overline{p}}{dx} = 0, \tag{5}$$

whose solution requires: (1) Two boundary conditions, (2) a model for the diffusivity K_M, and (3) an estimate for the drag coefficient C_D.

5.1.1. *Eddy diffusivity and mixing length*

The simplest model for the eddy diffusivity, which is a variant on the von Kármán–Prandtl mixing-length theory, is given by

$$K_M = l_{\text{eff}}^2 \left|\frac{d\overline{u}}{dz}\right|, \tag{6}$$

where l_{eff} is the effective mixing length. In order to parameterize l_{eff} as a function of the established vortex sizes, we consider again the three regions described earlier.

In Region III, the classical Monin–Obukhov similarity theory leads to

$$l_{\text{eff}} = l_{BL} = k\, L_{BL} = k(z - d). \tag{7}$$

The zero plane displacement, d, can be evaluated by the centre-of-pressure method (Thom, 1971; Jackson, 1981) given by

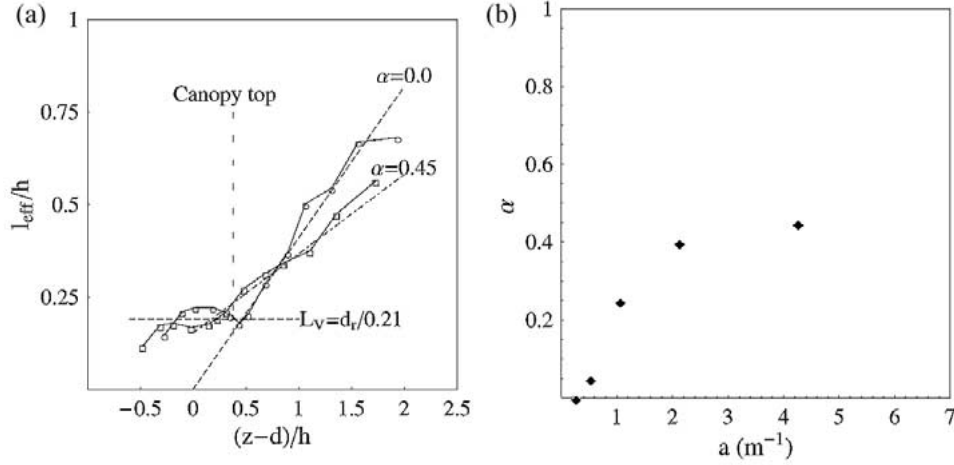$$d = \frac{\int_0^h zF(z)dz}{\int_0^h F(z)dz}. \tag{8}$$

Figure 8. The computed mixing length for sparsest and densest canopies, (a) l_{eff} using the measurements (symbol as in Figure 3) and predicted values from the conceptual model (broken lines). (b) The α coefficients are evaluated from the measured data.

In Region I, the mixing length is connected with the size of the characteristic vorticity L_V. The values of l_{eff}, evaluated from the experimental data (combining and inverting (6) and (4)), are shown in Figure 8. From this comparison it is evident that the mixing length and L_V are approximately equivalent.

In Region II, the flow field is a superposition of the classical boundary layer and a mixing layer. A linear superposition model for the mixing length is proposed here as

$$l_{\text{eff}}(z) = (1 - \alpha)l_{BL}(z) + \alpha l_{ML}, \tag{9}$$

where α ranges between 0 to 1, depending on the relative contribution of boundary-layer eddies and mixing layer eddies to the net vertical transport of momentum.

The mixing length of the plane mixing layer l_{ML} requires further parameterization in terms of variables that are computed by the closure model. The length L_s (as used in (4)) is problematic because it requires a priori knowledge of the mean velocity and the velocity gradients near the canopy top, which are precisely what the closure model is solving for. More appropriate would be an estimate of l_{ML} that is a direct function of canopy density and basic velocity scales. In Appendix A we provide support for the use of

$$l_{ML} = \frac{2}{\widehat{C_D a}} \left(\frac{u_*}{\overline{u}_h} \right)^2, \tag{10}$$

where $\widehat{C_D a}$ is the canopy depth-averaged $C_D a$. Furthermore, $u_*/\overline{u}$ is known to vary systematically with canopy density (Raupach, 1994). The proposed parameterization of $u_*/\overline{u}$ in terms of a is presented in Appendix A. Hence, both l_{BL} and l_{ML}

can be estimated without a priori knowledge of the mean velocity profile. We note that Equation (10) suffers from a singularity as $\widehat{C_D a}$ becomes negligible. However, as $a \to 0$ the inflection in the velocity profile vanishes and the Kelvin–Helmholtz mechanism is no longer relevant.

The l_{eff} values derived from the extreme (sparsest and densest) canopy cases are shown in Figure 8a. Through linear regression of the experimental data (over Regions I and II), the values of the coefficient α are evaluated. Such a regression was performed for all five cases, with the resulting α values plotted against a in Figure 8b. It appears that the function is well covered by the five model canopy densities, with an apparent asymptotic value of about 0.5. An important consequence of α not being unity for dense canopies is that the end-member flow over the densest cases is not a pure mixing layer, but rather an even combination of both flow types.

A further implication of the results in Figure 8 is that the effective mixing length for the region just above the canopy, $1 < z/h < 2$, is enhanced above its value predicted by the classical Monin–Obukhov similarity by a factor of up to 1.5. This enhancement in length scale leads to a linear enhancement in momentum diffusivity, which is consistent with numerous observations that the flow near $z/h = 1$ appears more diffusive than that predicted by surface-layer similarity theory (Thomson, 1979; Raupach, 1979; Garratt, 1980; Kaimal and Finnigan, 1994; Raupach et al., 1996; Finnigan, 2000; Novak et al., 2000).

For modelling purposes, Figure 8 provides some guidelines about the extent of these regions. Based on this figure, Region I extends up to $(z - d)/h = 0.5$ for the sparsest canopy and 0.2 for the densest canopy. Region II extends up to $(z - d)/h = 1.3$ for all canopy densities.

5.1.2. *Drag coefficient*

The main difficulty in estimating C_D, a key parameter in the mean momentum equation, is the sheltering effect (of consecutive obstacle elements) and its dependence on the local element Reynolds number, as discussed in Raupach and Thom (1981), Brunet et al. (1994) and Finnigan (2000). By combining the aerodynamic force per unit volume parameterized in Equation (3), and the simplified mean momentum equation, we obtain

$$C_D(z, Re, a) = -2 \left(\frac{\mathrm{d}\overline{(u'w')}}{\mathrm{d}z} + \frac{\mathrm{d}\overline{p}}{\mathrm{d}x} \right) \left(a\, \overline{u}^2 \right)^{-1} . \tag{11}$$

From the measured profiles of $\overline{u'w'}$, and $\overline{u}$, C_D is computed and shown in Figure 9a.

The general trend is that C_D decreases with increasing distance from the wall and increases with increasing a. The increase with a is inconsistent with the wind-tunnel experiments reported by Novak et al. (2000) who found the opposite trend. The Novak et al. experiments differ from ours in that, (i) u_* was held constant, while ours vary (see Table I), and (ii) the canopy was composed of plastic trees
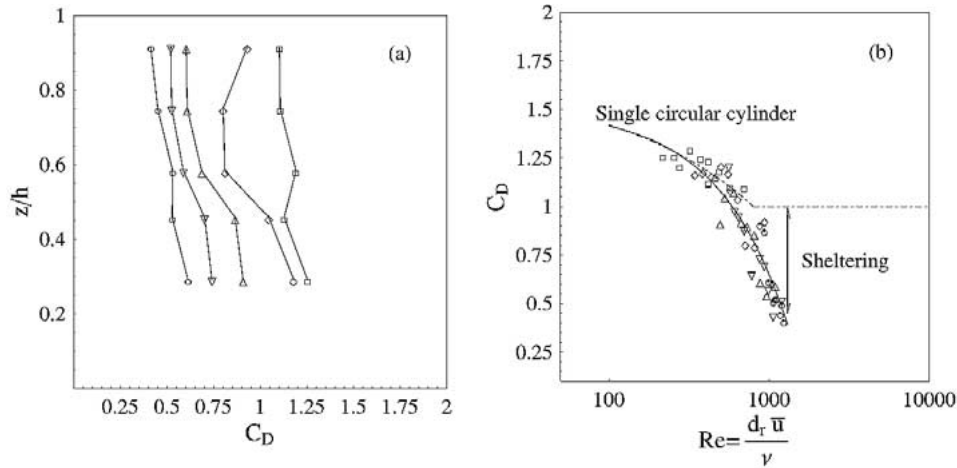
Figure 9. Drag coefficients, C_D, plotted versus the normalized distance from the wall (z/h) (a) and versus the Reynolds number $Re = d_r\overline{u}/\nu$ (b). The expected values for a singular cylinder (broken line) and from Equation (12) (solid line) are also shown.

(i.e., more than one scale that sheds vorticies) and not 'identical' cylinders as is in our experiment. It is likely that these two factors contributed to drag coefficient differences between our experiment and the Novak et al. experiments though this issue needs further exploration.

When all C_D measurements are combined and plotted as a function of the local element Reynolds number Re_d (Figure 9b), a clear relationship emerges. At low Reynolds numbers, the C_D is consistent with the classical behaviour of drag on a unit length of an isolated cylinder (i.e., $C_D \simeq Re^{1/2}$, Bachelor, 1954). With increasing Reynolds number, the C_D values monotonically decrease (rather than attain a constant value, as for an isolated cylinder). This decrease is attributed to the sheltering effect, which injects a persistent Reynolds number dependence in C_D even for large Reynolds numbers. Interestingly, the computed values here for the high Reynolds numbers are in agreement with several observed drag coefficients reported for field and wind-tunnel studies (Thom, 1971; Seginer et al., 1976; Brunet et al., 1994). Figure 9b also demonstrates that variations in canopy density have a minor impact on C_D when compared to variations in the local element Reynolds number, at least for our canopy flow configuration. From our experiments, C_D is approximately described by a linear function of Re_d, given by

$$C_D(Re_d) = -8.5 \times 10^{-4} Re_d + 1.5. \tag{12}$$

This relationship is empirical and requires further testing for other canopy configurations before any universality can be inferred. In fact, when taken together with the Novak et al. wind-tunnel study, the largest uncertainty one must face in modelling momentum transfer inside canopies is the drag coefficient.

5.2. BOUNDARY CONDITIONS

To solve Equation (5) numerically, two boundary conditions must be specified. The velocity at the farthest point from the wall was evaluated by the classical logarithmic velocity profile and the velocity at $z \to 0$ was evaluated from considerations of the local momentum balance. Near the wall, we assume that the magnitude of the stress divergence is small compared to the local drag force, and therefore, it is possible to evaluate a 'free-slip' velocity from Equations (2) and (3) near the boundary as

$$\overline{u}_{z \to 0} = \left(\frac{2 \mathrm{d} \overline{p}/\mathrm{d}x}{C_D a} \right)^{1/2}. \tag{13}$$

The upper boundary condition was set at $z/h = 2$ to avoid errors associated with the observed nonlinearity of $\overline{u'w'}$ in the region near the air-water interface.

5.3. COMPARISON WITH MEASUREMENTS

The measured and modelled $\overline{u}$ and $\overline{u'w'}$ are compared in Figure 10. In these calculations, a cubic spline was used to interpolate l_{eff} between regions I and II. Vertical axes are scaled with h, the Reynolds stress profiles are scaled with u_*^2, and the mean velocity profiles are scaled with u_* (which is different scaling from Figure 3a). The closure model, with its combination of a simple linear superposition mixing length and a drag coefficient that is linear in Re_d, yields results that agree well with the measurements. The model captures the increasing inflection in the mean velocity profile with increasing canopy density. Furthermore, the model correctly predicted stronger attenuation in the Reynolds stress profile with increasing a. The good agreement between model calculations and measurements for such a wide range of canopy roughness density suggests that the proposed mixing-length model for the three regions and the linear dependence C_D on Re_d can be used with some confidence to connect the canopy roughness density with CSL flows.

6. Conclusions

The structure of CSL turbulence was investigated using spatial and high-resolution temporal LDA measurements conducted in a flume for a wide range of canopy densities. The spectral measurements clearly suggest that for $z/h \ll 1$, the flow is primarily dominated by small vortices associated with the von Kármán streets. A phenomenological model was presented, in which the CSL is comprised of three layers. In the lowest layer (I), deep within the canopy, the flow is dominated by von Kármán streets. In the middle layer (II), spanning the canopy top, the flow is a superposition of a mixing layer and a rough-wall boundary layer. The upper layer (III) is described by the classical boundary-layer formulation. This 3-layer
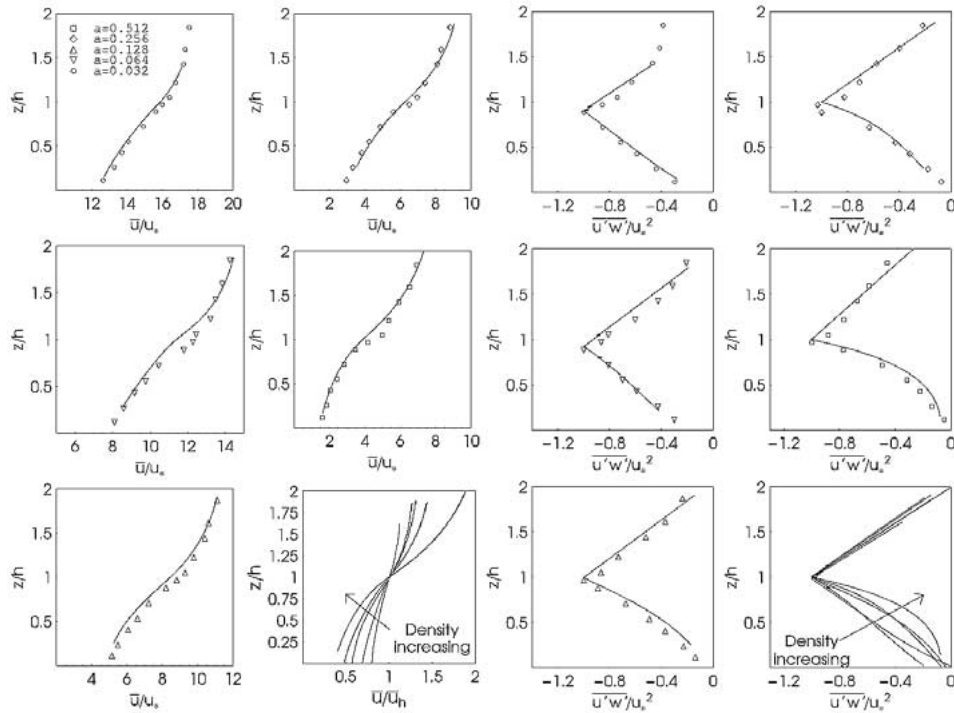
Figure 10. Comparison between measured and predicted (solid line) mean velocity and Reynolds stresses for five canopy densities. Top panel is for sparse, and bottom panel is for dense, the symbols are as in Figure 3.

formulation is consistent with a number of observed features for CSL turbulence, namely: Short-circuiting of the energy cascade in the deeper layers of the canopy (I), enhanced diffusivity in momentum flux near the canopy-atmosphere interface (II), and the convergence to Monin–Obukhov similarity forms in the upper region (III).

With the advancement of remote sensing technology (e.g., laser altimetry) it is likely that broad space-time data mapping of canopy roughness densities should become readily available. The proposed mixing-length model here will provide a mechanistic bridge from the roughness density maps to vertical transport predictions, because it is tied more closely to the mechanics of CSL transport.

Acknowledgements

(BER) Program, U.S. Department of Energy, through the Southeast Regional Center (SERC) of the National Institute for Global Environmental Change (NIGEC), and through the Terrestrial Carbon Processes Program (TCP) and the FACE project.

Appendix A

To establish a relationship between l_{ML} and canopy density, we assume an analytic expression for the mean velocity and then proceed to use the mean momentum balance. The most popular expression for the mean velocity profile within the canopy is given by

$$\overline{u}(z) = \overline{u}(h)e^{\beta(z/h-1)}, \tag{A1}$$

where β is the attenuation coefficient (Campbell and Norman, 1998). Starting with the definition of L_s and using the exponential mean velocity profile,

$$L_s = \left.\frac{\overline{u}(z)}{d\overline{u}/dz}\right|_{z=h} = \frac{h}{\beta}. \tag{A2}$$

In the absence of a pressure gradient, and upon integrating the mean momentum balance, we obtain

$$\overline{u'w'}(h) - \overline{u'w'}(0) = -\int_0^h C_d \, a \, \overline{u}^2(h) \, e^{2\beta(z/h-1)}dz, \tag{A3}$$

where $\overline{u'w'}(h) = -u_*^2$. Assuming that for dense canopies all the momentum is absorbed by the canopy (i.e., $\overline{u'w'}(0) \approx 0$), and that $(C_D a)$ is approximately constant with height given by $\widehat{C_D a}$, Equation (A3) reduces to

$$\frac{\beta}{h} = \frac{1}{2} \, \widehat{C_D a} \, \left(\frac{\overline{u}(h)}{u_*}\right)^2 \, \left(1 - e^{-2\beta}\right). \tag{A4}$$

Within canopies, the maximum depth of the mixing layer is bounded by the canopy height, thus making $\beta > 1$. With $\beta > 1$, $e^{-2\beta}$ becomes $\ll 1$ and

$$L_s \approx \frac{2}{\widehat{C_D a}} \, \left(\frac{u_*}{\overline{u}(h)}\right)^2. \tag{A5}$$

One remaining unknown in the above formulation is the variation in $u_*/\overline{u}(h)$. Typically, $u_*/\overline{u}(h)$ is not a priori known but it can be estimated from a as shown in Raupach (1994). To illustrate, we computed $u_*/\overline{u}(h)$ from the measurements reported in Figure 3 and further demonstrated in Figure A1 as an over-all good agreement with the data reported in Raupach (1994).
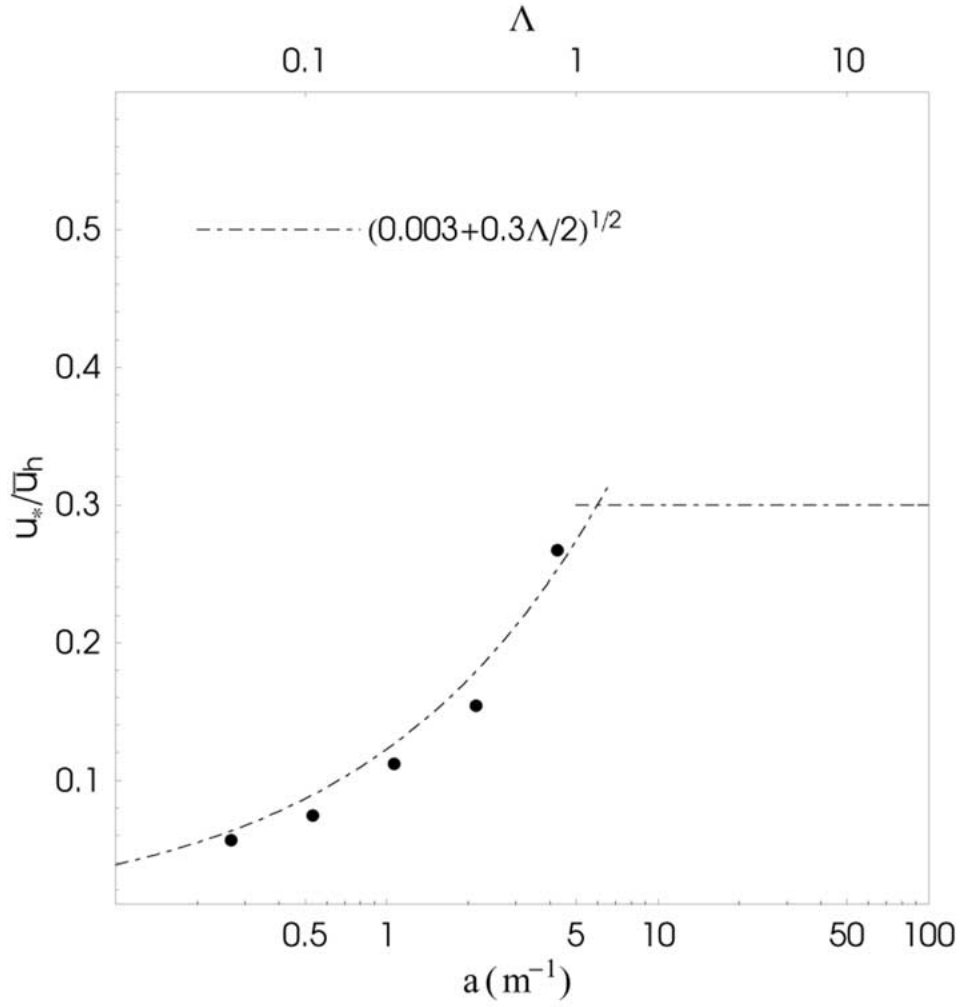
Figure A1. Variation in $\overline{u}_*/u_h$ with canopy area index (Λ) or element area index (a). The broken lines are from Raupach (1994) and the symbols are evaluated from the data.

To explore whether the estimate of L_s is sensitive to our assumption of an exponential mean velocity profile, we repeated the entire derivation using

$$\overline{u}(z) = \overline{u}(h)(1 + \tanh[\beta(z - h)]) \tag{A6}$$

and found that when $\beta > 1$,

$$L_s \approx \frac{2.6}{\widehat{C_D a}} \left(\frac{u_*}{\overline{u}(h)}\right)^2, \tag{A7}$$

which is almost identical to the result obtained from the exponential mean velocity profile. Hence, our estimate of L_s is not overly sensitive to our choice of an exponential $\overline{u}(z)$.

References

Antonia, R. A.: 2001, 'Reynolds-Number Dependence of High-Order Moments of the Streamwise Turbulent Velocity Derivative', *Boundary-Layer Metereol.* **21**, 159–171.

Batchelor, G. K.: 1967, *An Introduction to Fluid Dynamics*, Cambridge University Press, 615 pp.

Brunet, Y., Finnigan, J. J., and Raupach, M. R.: 1994, 'A Wind Tunnel Study of Air Flow in Waving Wheat: Single-Point Velocity Statistics', *Boundary-Layer Meteorol.* **70**, 95–132.

Finnigan, J.: 2000, 'Turbulence in Plant Canopies', *Annu. Rev. Fluid Mech.* **32**, 519–571.

Garratt, J. R.: 1980, 'Surface Influence upon Vertical Profiles in the Atmospheric Near Surface Layer', *Quart. J. Roy. Meteorol. Soc.* **106**, 803–819.

Harding, D., Lefsky, M. A., Parker, G. G., and Blair, B.: 2001, 'Laser Altimetry Canopy Height Profiles: Methods and Validation for Closed-Canopy, Broadleaved Forests', *Remote Sens. Environ.* **76**, 283–297.

Horn, H. S., Nathan, R., and Kaplan, S. R.: 2001, 'Long-Distance Dispersal of Tree Seeds by Wind', *Ecol. Res.* **16**, 877–885.

Jackson, P. S.: 1981, 'On the Displacement Height in the Logarithmic Velocity Profile', *J. Fluid Mech.* **111**, 15–25.

Kaimal, J. C. and Finnigan, J. J.: 1994, *Atmospheric Boundary Layer Flows: Their Structure and Measurement*, Oxford University Press, 289 pp.

Katul, G. G. and Albertson, J. D.: 1998, 'An Investigation of Higher Order Closure Models for a Forested Canopy', *Boundary-Layer Metereol.* **89**, 47–74.

Katul, G. G., Geron, C. D., Hsieh, C. I., Vidakovic, B., and Guenther, A. B.: 1998, 'Active Turbulence and Scalar Transport near the Land-Atmosphere Interface', *J. Appl. Meteorol.* **37**, 1533–1546.

Lefsky, M. A., Cohen, W. B., Harding, D. J., and Parker, G. G.: 2002, 'Lidar Remote Sensing for Ecosystem Studies', *Bioscience* **52**, 19–30.

Lu, S. S. and Willmarth, W. W.: 1973, 'Measurements of the Structure of Reynolds Stress in a Turbulent Boundary Layer', *J. Fluid Mech.* **60**, 481–571.

Marshall, B. J., Wood, C. J., Gardiner, B. A., and Belcher R. E.: 2002, 'Conditional Sampling of Forest Canopy Gusts', *Boundary-Layer Meteorol.* **102**, 225–251.

Nakagawa, H. and Nezu, I.: 1977, 'Prediction of the Contributions to the Reynolds Stress from Bursting Events in Open Channel Flows', *J. Fluid Mech.* **80**, 99–128.

Nathan, R., Katul, G. G., Horn, H. S., Thomas, S. M., Oren, R., Avissar, R., Pacala, S. W., and Levin, S. A.: 1977, 'Mechanisms of Long-Distance Dispersal of Seeds by Wind', *Nature* **418**, 409–413.

Novak, M. D., Warland, J. S., Orchansky, A. L., Ketler, R., and Green, S.: 2000, 'Comparison between Wind Tunnel and Field Measurements of Turbulent Flow. Part 1: Uniformly Thinned Forests', *Boundary-Layer Meteorol.* **95**, 457–495.

Poggi, D., Porporato, A., and Ridolfi, L.: 2002, 'An Experimental Contribution to Near-Wall Measurements by Means of a Special Laser Doppler Anemometry Technique', *Exp. Fluids* **32**, 366–375.

Raupach, M. R.: 1979, 'Anomalies in Flux-Gradient Relationships over Forest', *Boundary-Layer Meteorol.* **16**, 467–486.

Raupach, M. R.: 1981, 'Conditional Statistics of Reynolds Stress in Rough-Wall and Smooth-Wall Turbulent Boundary Layers', *J. Fluid Mech.* **108**, 363–382.

Raupach, M. R.: 1994, 'Simplified Expressions for Vegetation Roughness Length and Zero-Plane Displacement as Functions of Canopy Height and Area Index', *Boundary-Layer Meteorol.* **71**, 211–216.

Raupach, M. R. and Shaw, R. H.: 1982, 'Averaging Procedures for Flow within Vegetation Canopies', *Boundary-Layer Meteorol.* **61**, 47–64.

Raupach, M. R. and Thom, A. S.: 1981, 'Turbulence in and above Plant Canopies', *Annu. Rev. Fluid. Mech.* **13**, 97–129.

Raupach, M. R., Finnigan, J. J., and Brunet, Y.: 1996, 'Coherent Eddies and Turbulence in Vegetation Canopies: The Mixing Layer Analogy', *Boundary-Layer Meteorol.* **78**, 351–382.

Scanlon T. M., Albertson, J. D., Caylor, K. K., and Williams, C. A.: 2002, 'Determining Land Surface Fractional Cover from NDVI and Rainfall Time Series for a Savanna Ecosystem', *Remote Sens. Environ.* **82**, 376–388.

Schlichting, H.: 1979, *Boundary-Layer Theory*, McGraw-Hill, 817 pp.

Seginer, I., Mulhearn, P. J., Bradley, E. F., and Finnigan, J. J.: 1976, 'Turbulent Flow in a Model Plant Canopy', *Boundary-Layer Meteorol.* **10**, 423–453.

Thom, A. S.: 1971, 'Momentum Absorption by Vegetation', *Quart. J. Roy. Meteorol. Soc.* **97**, 414–428.

Thomson, N.: 1979, 'Turbulence Measurements above a Pine Forest', *Boundary-Layer Meteorol.* **16**, 293–310.